Retrieving Oil-Water Mixture Ratios of Marine Oil Spills From L-Band SAR Imagery

Honglei Zheng, Chunyu Gou, Ali Khenchaf, Yunhua Wang, Yanmin Zhang

Retrieving Oil-Water Mixture Ratios of Marine Oil Spills From L-Band SAR Imagery

Honglei Zheng, *Member, IEEE*, Chunyu Gou, Ali Khenchaf, Yunhua Wang, and Yanmin Zhang

***Abstract*— Retrieving the oil-water mixture ratio (*M*, the proportion of oil in an oil-water mixture) of the marine oil spill is of vital importance for the emergency treatment of oil pollution, which can be achieved by a copolarization ratio (PR) method. In the framework of the PR method, it is assumed that Bragg scattering dominates at moderate incidence angles, and the relative contribution of non-Bragg scattering to total scattering (RCNT) is typically neglected. However, in this work, it is found that the RCNT cannot be neglected for L-band, especially for HH polarization at higher wind speeds (the RCNT is approximately 0.6–0.8 for wind speeds of 10–12 m/s). The significant impact of non-Bragg scattering results in the PR method not being accurate enough for retrieving *M*. After separately investigating the influences of the damping effect and effective dielectric constant reduction on the RCNT, a novel approach is proposed for more accurately estimating the *M* of marine oil spills by eliminating the impact of non-Bragg scattering. The proposed method was applied to uninhabited aerial vehicle synthetic aperture radar (UAVSAR) images collected during the Deepwater Horizon (DWH) oil spill accident. The inversion results of our approach show that the *M* of most oil spill areas ranges from approximately 0.3 to 0.6, which matches the reality better than that of a traditional PR method (ranging from approximately 0.6 to 0.8).**

***Index Terms*— Non-Bragg scattering, ocean oil spill, oil-water mixture ratio, synthetic aperture radar (SAR).**

I. Introduction

THE frequently occurring marine oil spill accidents seriously harm the marine environment and marine life. Once oil spill accidents occur, under the action of wind shear stress, turbulence, waves, and other dynamic factors in the marine environment, crude oil and seawater mix together and form different concentrations of oil spill emulsions [1]. For oil spill emulsions with different oil-water mixture ratios (*M*, the proportion of oil in an oil-water mixture), different emergency treatment strategies need to be adopted, such as combustion elimination, absorbent felt adsorption, dispersants spraying, and oil skimmer recovery. Therefore, accurate quantification of the *M* of oil spill emulsions is of great significance for the emergency treatment of oil spill pollution [2].

Synthetic aperture radar (SAR) is one of the most effective tools for observing marine oil spills, as it provides valuable data under all-weather, all-day, and all-night conditions [3], [4], [5]. It is well known that an oil spill on the sea surface appears as a "dark patch" in a SAR image. This is because the oil spill attenuates the intensity of SAR backscattering by damping small-scale waves and reducing the effective dielectric constant. Specifically, on the one hand, oil films on the sea surface decrease sea surface tension, wind friction, and growth and increase wave dissipation, resulting in the remarkable suppression of capillary and short-gravity sea waves. These capillary and short-gravity sea waves govern microwave backscattering [6]. On the other hand, the effective dielectric constant of an oil spill-covered sea surface is significantly lower than that of the clean sea surface when the oil film is sufficiently thick or mixed with seawater [2], [5].

In recent decades, extensive effort has been devoted to distinguishing oil spills from look-like oil spills (such as biological oil films and low wind areas) by using SAR, e.g., [7], [8], [9]. In recent years, scientists have gradually realized the importance of the quantitative detection of the oil-water mixture ratio (or oil concentration) for oil spill emergency treatment and disaster assessment. Minchew proposed an oil/seawater mixing index (Mdex), which can be used to characterize the oil and seawater mixing type [10]. A positive Mdex indicates that the attenuation of the radar backscattering from the oil-covered sea surface is mainly caused by the suppressed surface roughness. Whereas a negative Mdex indicates that the decreased radar backscattering is mostly induced by the reduced relative complex permittivity of the oil/water mixture. In his work, the copolarization ratio (PR) was used to decouple the surface roughness damping and reduction in the relative complex permittivity, which both relate to radar backscattering attenuation. Later, Collins et al. [11] used the Mdex to characterize oil and seawater mixing types based on simulated compact polarimetric SAR data. Based on L-band SAR images, Angelliaume et al. [12] developed a simple PR method to quantify the oil concentration of pollutants on the ocean surface that does not rely on clean sea surfaces A similar

This work was supported in part by the National Natural Science Foundation of China under Grant 52101393, in part by the Joint Funds of the National Natural Science Foundation of China under Grant U2006207, and in part by the Natural Sci-ence Foundation of Shandong Province, China under Grant ZR2021QD001.

Honglei Zheng and Yanmin Zhang are with the Faculty of Information Science and Engineering, Ocean University of China, Qingdao 266100, China (e-mail: hongleizheng@hotmail.com; yanminzhang@ouc.edu.cn).

Chunyu Gou is with the College of Oceanography and Space Informatics, China University of Petroleum (East China), Qingdao 266580, China (e-mail: s21160023@s.upc.edu.cn).

Ali Khenchaf is with the Lab-STICC, UMR CNRS 6285, ENSTA Bretagne, 29806 Brest, France (e-mail: ali.khenchaf@ensta-bratagne.fr).

Yunhua Wang is with the Faculty of Information Science and Engineering, Ocean University of China, Qingdao 266100, China, and also with the National Laboratory for Marine Science and Technology, Qingdao 266237, China (e-mail: yunhuawang@ouc.edu.cn)

PR method was also used by Li et al. [2] to retrieve the oil-water mixture ratio from simulated L-band compact polarized SAR images. Experimental results showed that the oil-water mixture ratios obtained from compact polarized SAR data are in overall agreement with those obtained from fully polarized SAR data. Based on the physical modeling of electromagnetic scattering from an oil-covered sea surface, Boisot et al. demonstrated a marine oil slick quantification method. The quantification method utilized the L-band PR properties to estimate the volume fraction and the complex effective permittivity of a water-in-oil mixture from L-band dual-polarization SAR imagery [13]. Recently, Quigley et al. proposed retrieving the dielectric parameters of oil slicks from C-band SAR images based on the PR derived from a polarimetric two-scale surface scattering model. Their results demonstrated that this method can provide a reasonable estimation for the dielectric parameters [14], [15]. Since the dielectric properties directly depend on the oil-water mixture ratio, retrieving the dielectric properties is equivalent to retrieving the oil-water mixture ratio of oil spills.

The exploitation of polarimetric SAR to observe marine oil spills and infer quantitative information has also been carried out. In [16], polarimetric features derived from the Mueller matrix were used to observe sea oil spills in L- and C-band SAR images. It was found that these polarimetric features can emphasize (deemphasize) the presence of oil slicks (weakly damping surfactants) with respect to the background sea. In [17], full-polarimetric L-band uninhabited aerial vehicle synthetic aperture radar (UAVSAR) and C-band RADARSAT-2 SAR data were shown to be effective in observing surfactants at sea and analyzing the spatial variability of the damping properties related to the Deepwater Horizon (DWH) surfactants. As stated, once properly modeled, polarimetric SAR data not only allow identifying polluted areas but also support a preliminary classification of surfactants according to their damping properties. In [18], the effect of the dielectric properties of an oil-in-water mixture on the corresponding polarimetric backscattering was studied through analysis of a marine oil seep. It was shown that the backscattering from an oil seep is affected by the oil's damping properties more than its concentration in the water column.

In the above works, it was assumed that the Bragg scattering dominates at moderate incidence angles and that the impact of non-Bragg scattering is negligible. In this case, the PR derived from a SAR image can be simplified as the Bragg polarization ratio (BPR), which is independent of the surface roughness or the ocean wave spectra, and merely depends on incidence angles and the complex dielectric constant of the medium [2], [13], [19]. However, as reported, non-Bragg scattering, which is related to quasi-specular backscattering from the steep forward faces of breaking or near-breaking waves [20], edge diffraction from sharply crested waves [21], etc., also has a significant impact on radar scattering. This means that the accuracy of the inverted M based on the PR method may be significantly influenced by the non-Bragg scattering. The main purpose of this article is to evaluate the influence of non-Bragg scattering on L-band radar scattering and to develop a more accurate method for retrieving M by eliminating the influence of non-Bragg scattering.

This article is organized as follows: First, the backgrounds of microwave scattering from sea surfaces and L-band SAR data used in this article are introduced in the second and third parts, respectively. Then, the fourth part presents some results and discussions. Finally, a conclusion to this article is provided in the fifth part.

II. Theory and Methodology

A. Bragg and Non-Bragg Scattering From the Sea Surface

At moderate incidence angles (usually 30°–60°), the total normalized radar cross section (NRCS, $\sigma_{\rm pp}$) of the sea surface can be represented as a sum of Bragg scattering ($\sigma_{\rm pp}^{B}$) and non-Bragg scattering ($\sigma^{\rm nB}$) [20]

$$\sigma_{\rm pp} = \sigma_{\rm pp}^{B} + \sigma^{\rm nB} \tag{1}$$

where the subscript pp indicates either horizontal-horizontal (HH) or vertical-vertical (VV) polarizations. It should be noted that $\sigma_{\rm pp}^{B}$ depends on the polarization and that $\sigma^{\rm nB}$ is independent of polarization. In this article, the PR refers to $\sigma_{\rm HH}/\sigma_{\rm VV}$, and the BPR refers to $\sigma_{\rm HH}^{B}/\sigma_{\rm VV}^{B}$.

The Bragg scattering component is usually modeled by the two-scale model (TSM), and then the NRCS of the Bragg scattering can be expressed as [20]

$$\sigma_{\rm pp}^{B} = \frac{\pi}{\tan^4\theta_i}\left|G_{\rm pp}\right|^2\left(1+g_{\rm pp}s_i^2\right)B(k_{\rm br},\phi) \tag{2}$$

where θ_i is the incidence angle, $g_{\rm pp}$ is the polarization-dependent coefficient, and

$$\begin{cases} G_{\rm VV} = \dfrac{(\varepsilon_{\rm sw}-1)\times\left[\varepsilon_{\rm sw}\left(1+\sin^2\theta_i\right)-\sin^2\theta_i\right]}{\left[\varepsilon_{\rm sw}\cos\theta_i+\sqrt{\varepsilon_{\rm sw}-\sin^2\theta_i}\right]^2} \\ G_{\rm HH} = \dfrac{\varepsilon_{\rm sw}-1}{\left[\cos\theta_i+\sqrt{\varepsilon_{\rm sw}-\sin^2\theta_i}\right]^2} \end{cases} \tag{3}$$

$$\begin{cases} g_{\rm VV} = \dfrac{\tan^4\theta_i}{2|G_{\rm VV}|^2}\dfrac{\partial^2}{\partial\theta_i^2}\left(\dfrac{|G_{\rm VV}|^2}{\tan^4\theta_i}\right) \\ g_{\rm HH} = \dfrac{\tan^4\theta_i}{2|G_{\rm HH}|^2}\dfrac{\partial^2}{\partial\theta_i^2}\left(\dfrac{|G_{\rm HH}|^2}{\tan^4\theta_i}\right)+\dfrac{2}{\sin^2\theta_i}\left|\dfrac{G_{\rm VV}}{G_{\rm HH}}\right|\dfrac{s_n^2}{s_i^2} \end{cases} \tag{4}$$

where $\varepsilon_{\rm sw}$ is the relative dielectric constant of seawater. The Bragg wavenumber is $k_{br} = 2k_i\sin\theta_i$, and k_i is the radar wavenumber. $B(k_{\rm br},\phi)$ is the directional curvature spectrum, and ϕ is the wave propagation direction with reference to the wind. Please note that throughout this work, as will be explained in Section II-B, we do not need to explicitly specify the form of the directional curvature spectrum.

In (2) and (4), s_i^2 and s_n^2 are the mean square slope (MSS) of tilting waves in and out of the direction of the incidence plane, respectively. According to the measurements from [22], the slopes of waves in the slick-covered areas (the scales of these waves correspond to the scales of tilting waves in TSM) are almost isotropic. Following [23] and [24], we assume that $s_i^2 = s_n^2 = s^2/2$, and the MSS can be obtained by

$$s^2 = A\ln\left(k_d U_{10}^2/g\right) \tag{5}$$

where U_{10} is the wind speed at 10 m height, g is the gravity acceleration, and k_d is the wavenumber dividing the sea surface roughness into small- and large-scale components in the TSM. Equation (5) was obtained by integrating the Phillips wave slope spectrum [24] between k_d and k_0, where k_0 is the wavenumber at the energy peak, assumed to correspond to fully developed wind wave conditions ($k_0 \sim g/U_{10}^2$). The constant A is chosen here as '4.6×10^{-3}' as suggested by Phillips [24]. The k_d wavenumber can be arbitrarily chosen within wide limits. For instance, $k_d = k_{br}/4$ and $k_d = 2\pi/0.3$ are adopted in [23] and [24], respectively. According to our calculation, the impact of k_d on the following results of this article is negligible when k_d ranges from $k_{\mathrm{br}}/3$ to $k_{\mathrm{br}}/10$. In this work, $k_d = k_{br}/4$ is used in the following calculations and simulations.

The NRCS of non-Bragg scattering can be derived from dual copolarized NRCSs [23], [25]

$$\sigma^{\mathrm{nB}} = \sigma_{\mathrm{VV}} - \frac{\sigma_{\mathrm{VV}} - \sigma_{\mathrm{HH}}}{1 - r_B} \tag{6}$$

where r_B is estimated as the expected BPR, which can be obtained by

$$r_B = \frac{|G_{\mathrm{HH}}|^2\left(1 + g_{\mathrm{HH}} \times s_i^2\right)}{|G_{\mathrm{VV}}|^2\left(1 + g_{\mathrm{VV}} \times s_i^2\right)}. \tag{7}$$

To estimate the impact of non-Bragg scattering on total scattering, the relative contribution of non-Bragg scattering to total scattering (RCNT) is defined as

$$c_{\mathrm{pp}}^{\mathrm{nB}} = \frac{\sigma^{\mathrm{nB}}}{\sigma_{\mathrm{pp}}}. \tag{8}$$

B. Quantitatively Estimating the Impacts of the Damping Effect and Effective Dielectric Constant Reduction Induced by Emulsions (or Oil-Water Mixtures) With Different M Values on RCNT

In previous works, the impacts of various surface ocean phenomena on non-Bragg scattering, such as ocean currents, slicks, wind fields, and internal waves, have already been studied [26], [27]. However, the influences of oil emulsions (or oil-water mixtures) with different M values on non-Bragg scattering have not been well studied. Typically, an oil spill in the marine environment behaves in two ways. It can either float on the sea surface as a thin film or mix with seawater within the water column. Correspondingly, an oil spill attenuates radar backscattering in two ways: by damping small-scale sea waves and by reducing the effective dielectric constant [5], [10], [13], [28]. Considering that the impact of non-Bragg scattering on microwave scattering is important, the RCNTs in the above two cases are discussed in this article. In the following, methods to quantify the impacts of the damping effect and effective dielectric constant reduction induced by emulsions with different M values on the RCNT are introduced in detail.

When the sea surface is covered with a thin oil film/emulsion, small-scale waves are damped (the high-frequency part of the curvature wave spectrum is modified as compared to the clean sea), the damping effect dominates for radar signal attenuation. This is because the thickness of the oil film floating on the sea surface (usually from μm to mm) is far smaller than the expected penetration depth of a radar (approximately 7–9 mm for clean water for the L-band) [29]. Thus, the influence of the change in the effective dielectric constant on radar scattering is negligible since scattering occurs mainly from the seawater interface [30]. In this case, the non-Bragg scattering NRCS can be calculated by (6) from dual copolarized SAR images, and the RCNT can be directly obtained by (8). Please note that a thin oil film/emulsion only damps the short-scale surface roughness (high-frequency part in the elevation spectrum). According to its definition, s^2 filters out the contribution of the highest frequencies (frequencies higher than those corresponding to k_d) which are those contributing the most to the MSS. Therefore, at least in L-Band, it can be considered that s^2 is similar within and outside the slick [14], even if the oil spill may affect the wave spectrum at the Bragg wavelength.

When the sea surface is covered with a thick emulsion (or oil-water mixture), both the damping effect and effective dielectric constant reduction may play important roles in radar signal attenuation because microwaves have difficulty penetrating the thick oil layer. The dielectric properties of the emulsion highly depend on M. Due to the unknown dielectric properties of a thick emulsion in a real case, the corresponding non-Bragg NRCS cannot be directly obtained by (6). In fact, it is not easy to separately analyze the influence of the reduction in the dielectric constant on RCNT because the impacts of the reduction in the dielectric constant and the damping effect on radar signal attenuation cannot be easily decoupled. Additionally, there are not enough field measurements to support this study. Under these circumstances, we perform this study based on theoretical simulations.

As stated above, the Bragg NRCS of a thick emulsion-covered sea surface can be simulated by (2). In this work, the curvature sea spectrum in (2) is derived from a real SAR image using

$$B(k_{\mathrm{br}}, \phi) = \frac{(\sigma_{\mathrm{VV}} - \sigma_{\mathrm{HH}})\tan^4\theta_i}{\pi\left[|G_{\mathrm{VV}}|^2\left(1 + g_{\mathrm{VV}}s_i^2\right) - |G_{\mathrm{HH}}|^2\left(1 + g_{\mathrm{HH}}s_i^2\right)\right]} \tag{9}$$

where σ_{HH}, σ_{VV}, and θ_i (of each pixel) are directly extracted along the white line in Fig. 1(c). Equation (9) can be easily obtained based on (1) and (2). The dielectric constant of seawater in (2) should be replaced by the effective dielectric constant of the emulsion. The effective dielectric constant of an oil emulsion can be estimated using the Bruggeman formula [29]

$$\varepsilon_{\mathrm{eff}} = \frac{1}{4}\Bigg\{\varepsilon_{\mathrm{sw}} - (1 - 3M)(\varepsilon_{\mathrm{oil}} - \varepsilon_{\mathrm{sw}}) + \sqrt{[\varepsilon_{\mathrm{sw}} - (1 - 3M)(\varepsilon_{\mathrm{oil}} - \varepsilon_{\mathrm{sw}})]^2 + 8\varepsilon_{\mathrm{sw}}\varepsilon_{\mathrm{oil}}}\Bigg\} \tag{10}$$

where M is the oil-water mixture ratio or oil content, and $\varepsilon_{\mathrm{oil}}$ is the dielectric constant of oil.

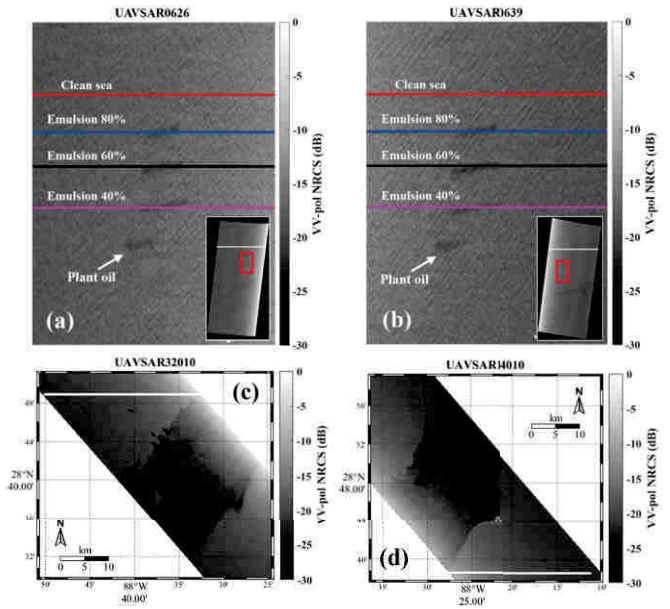

Fig. 1. (a) and (b) VV-polarized NRCS images of dataset (a). (c) and (d) VV-polarized NRCS images of dataset (b).

The non-Bragg NRCS of a thick emulsion-covered sea surface can be simulated by using [20], [25]

$$\sigma^{\mathrm{nB}} = q \cdot |R|^2 \sigma_0^{\mathrm{nB}}(\theta_i) \tag{11}$$

where

$$\sigma_0^{\mathrm{nB}}(\theta_i) = \left(\sec^4\theta_i / s_{\mathrm{wb}}^2\right) \exp\left(-\tan^2\theta_i / s_{\mathrm{wb}}^2\right) + \varepsilon_{\mathrm{wb}} / s_{\mathrm{wb}}^2 \tag{12}$$

$s_{\mathrm{wb}}^2 = 0.19$ and $\varepsilon_{\mathrm{wb}} = 0.005$ are empirical constants. Quantity q is the fraction of the sea surface covered by breaking zones, which depends on the radar wavelength. This parameter is described as an integral of the lengths of wave breaking fronts per unit surface expressed through the short wind wave spectrum. To take the dielectric properties of the emulsion into account, following [25], [31], we add the Fresnel reflection coefficient R here. R is related to the effective dielectric constant, which can also be obtained by (10). Finally, the RCNT can be obtained by $c_{\mathrm{pp}}^{\mathrm{nB}} = \sigma^{\mathrm{nB}}/(\sigma^{\mathrm{nB}} + \sigma_{\mathrm{pp}}^{B})$ under the condition that the reduction in the dielectric constant dominates the radar backscattering attenuation.

III. Dataset

The datasets used in this work were collected by UAVSAR, which is fully polarized SAR operating in the L-band. The center frequency of the incident wave is 1.2575 GHz. The UAVSAR data used in this work have three ranges (cross-track) and 12 azimuth (along the track) looks. The resolutions along the range and azimuth directions are 5 and 7.2 m, respectively.

Dataset (a) was collected at the abandoned Frigg field in the North Sea during the NORSE2015 experiment. The purpose of the NORSE2015 experiment was to study the dependence of varying oil-water mixtures on radar echoes. VV-polarized NRCS images of NORSE2015 UAVSAR data are provided, in dB scale, in Fig. 1(a) and (b). Fig. 1(a) was collected on 10 June 2015 at 06:26 universal time coordinated (UTC) and is hereafter referred to as UAVSAR0626. Fig. 1(b) was collected on 10 June 2015 at 06:39 UTC and is hereafter referred to as UAVSAR0639. Thumbnail views are shown in the lower right of Fig. 1(a) and (b). Four different dark patches can be observed in the scene that corresponds, from top to bottom, to an oil emulsion of 80% crude oil mixed with seawater (E80, $M = 0.8$), an emulsion of 60% crude oil mixed with seawater (E60, $M = 0.6$), an emulsion of 40% crude oil mixed with seawater (E40, $M = 0.4$) and plant oil. Dataset (a) is collected at a wind speed (U_{10}) of approximately 10–12 m/s. More details related to the NORSE2015 experiment can be found in [3] and [30]. Since the emulsion thickness was estimated in the range of 1.3–1.7 μm (significantly smaller than 7–9 mm, the penetration depth of L-band radar) during the NORSE2015 experiment, the impact of the reduction in the effective dielectric constant on microwave scattering is negligible [32]. Therefore, for dataset (a), the attenuation of the NRCS from the emulsion-covered areas in the SAR images is dominated by the damping effect. In this work, dataset (a) is used to study the impacts of thin emulsions (where the damping effect dominates) with different M values on RCNTs.

Dataset (b) was collected during the 2010 DWH oil spill accident. It is estimated that 7.0×10^5 m^3 of oil was released before the top was capped on July 15, 2010. In the DWH oil spill accident, the oil plume entrained water while the oil traveled from a depth of 1.7 km to reach the surface. Therefore, different from a thin oil film covering the sea surface, the upper layer of the oil spill sea surface was a mixture of water and oil. This means that both the damping effect and reduction in the effective dielectric constant may have induced radar signal attenuation. The VV-polarized NRCS images of the DWH oil spill UAVSAR data are provided, in dB scale, in Fig. 1(c) and (d). The flight line of Fig. 1(c) was gulfco-32010-10054-101-100623, and the data were collected on 23 June 2010 at 20:42 UTC, hereafter referred to as UAVSAR32010. The flight line of Fig. 1(d) was gulfco-14010-10054-100-100623, and the data were collected on 23 June 2010 at 21:08 UTC, hereafter referred to as UAVSAR14010. According to the observation of buoy #42012 (30°39′ N, 87°33′18″ W) and National Oceanic and Atmospheric Administration (NOAA) wave forecasts, dataset (b) was collected under the condition that the wind speed and wind direction of dataset (b) were about 2.5–5 m/s and 115°–126°, respectively [33].

The influence of noise is ignored because only the copolarized (HH and VV) NRCSs are used, and the copolarized NRCSs are much larger than the noise equivalent sigma zero (NESZ) when the incident angle is less than 60° [33].

IV. Results and Discussions

A. Impacts of Non-Bragg Scattering on L-Band Radar Scattering

The RCNT defined in (8) can be used to evaluate the impact of non-Bragg scattering on radar scattering, which is frequency-dependent [20], [34]. According to the study

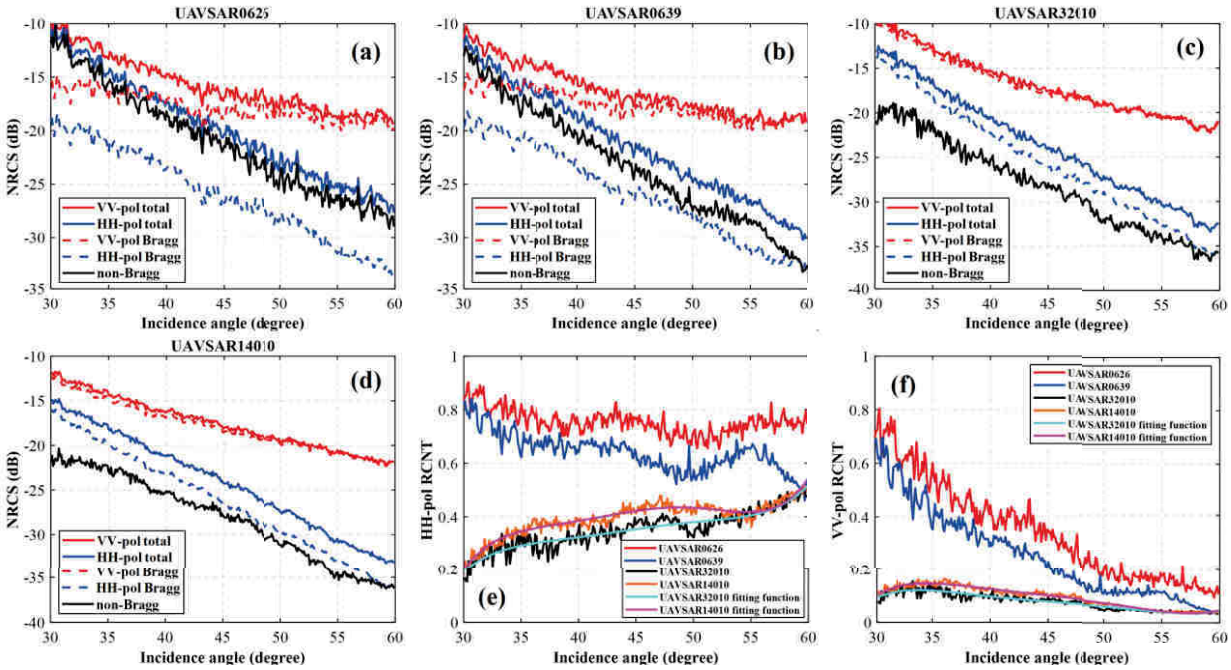

Fig. 2. NRCSs of the non-Bragg, Bragg and total scattering of clean sea surface calculated based on (a) UAVSAR0626, (b) UAVSAR0639, (c) UAVSAR32010, and (d) UAVSAR14010. The RCNTs were calculated from UAVSAR0626, UAVSAR0639, UAVSAR32010, and UAVSAR14010. (e) HH polarization. (f) VV polarization.

of [35], the contribution of non-Bragg scattering to total scattering is not significant at L-band. For instance, as suggested in [35], the RCNTs of VV and HH polarizations for a 20 m/s wind speed are 0.09 and 0.3, respectively, and they decrease with decreasing wind speed. In previous studies, by assuming that RCNT is negligible at lower frequencies (e.g., L-band), researchers have carried out the retrieval of the M of oil spills by using L-band SAR imagery [2], [10], [11], [12], [13], [15]. In the following, based on the datasets introduced in Section III, the property of RCNT is reanalyzed.

Fig. 2(a)–(d) presents the NRCSs of non-Bragg, Bragg, and total scattering obtained along the white lines in the thumbnail views of Fig. 1(a) and (b), and the white lines in Fig. 1(c) and (d). The VV- and HH-polarized total NRCSs are directly extracted along the white lines in Fig. 1. The non-Bragg scattering NRCSs are calculated by using (6) where σ_{VV} and σ_{HH} are the observations and r_B is estimated by (7) with a dielectric constant of clean seawater. In the calculation, the wind speeds are set to be the same as the wind speeds at the time the datasets were collected [$U_{10} = 5$ m/s for dataset (a) and $U_{10} = 12$ m/s for dataset (b)]. The wind speed is assumed to be constant over the whole image. The Bragg scattering NRCSs are calculated by $(\sigma_{\mathrm{pp}} - \sigma^{\mathrm{nB}})$ in linear units and presented in dB units. As shown in Fig. 2(a)–(d), the trends in non-Bragg, Bragg, and total NRCSs with the incident angle are the same. The non-Bragg NRCSs in Fig. 2(a) and (b) are larger than those in Fig. 2(c) and (d), indicating that the NRCSs of non-Bragg scattering increase with wind speed.

In Fig. 2(e) and (f), the RCNTs of dataset (a) are higher than those of dataset (b), indicating that the higher the wind speed is, the larger the RCNT. Moreover, the RCNT for HH polarization is significantly larger than that for VV polarization. These results are in agreement with the results achieved by [35]. Unexpectedly, as shown in Fig. 2(e) and (f), the HH-polarized and VV-polarized RCNTs for dataset (a) are, respectively, 0.5–0.8 and 0.1–0.8, and the HH-polarized and VV-polarized RCNTs for dataset (b) are, respectively, 0.2–0.5 and below 0.1. This means that the non-Bragg scattering makes a significant impact on L-band radar scattering.

According to (1), the total NRCS can be represented as the sum of Bragg scattering NRCS and non-Bragg NRCS. Hence the PR of a real SAR image can be written as

$$\frac{\sigma_{\mathrm{HH}}}{\sigma_{\mathrm{VV}}} = \frac{\sigma^B_{\mathrm{HH}} + \sigma^{\mathrm{nB}}}{\sigma^B_{\mathrm{VV}} + \sigma^{\mathrm{nB}}}. \tag{13}$$

It is known that the BPR $(\sigma^B_{\mathrm{HH}}/\sigma^B_{\mathrm{VV}})$ can be used for decoupling the damping effect and relative complex permittivity reduction, which both relate to radar backscattering attenuation. Since the influence of non-Bragg scattering on the total scattering is remarkable, the PR derived from UAVSAR images cannot be approximated to BPR (namely $(\sigma_{\mathrm{HH}}/\sigma_{\mathrm{VV}}) \neq (\sigma^B_{\mathrm{HH}}/\sigma^B_{\mathrm{VV}})$). Therefore, the PR cannot be used to decouple the two factors of the surface roughness damping and reduction in the relative complex permittivity accurately. To retrieve the M accurately, the impact of non-Bragg scattering on total scattering should be eliminated. However, at present, when the sea surface is covered with oil-water mixtures with different M values, the impacts of the damping effect and dielectric constant reduction on the RCNT are still not well understood.

B. Impacts of the Damping Effect Induced by Emulsions With Different M Values on RCNT

The impact of effective dielectric constant reductions on microwave scattering is negligible when the emulsion thickness is far smaller than the penetration depth of a radar.

Therefore, the influence of the damping effect induced by thin emulsions on the RCNT can be analyzed based on dataset (a). As the results of UAVSAR0626 and UAVSAR0639 are similar, only the results of UAVSAR0626 are shown in detail.

Fig. 3(a)–(c) shows the NRCSs in VV polarization of total scattering, Bragg scattering, and non-Bragg scattering correspond to the clean sea [along the red line in Fig. 1(a)], E80 [along the blue line in Fig. 1(a)], E60 [along the black line in Fig. 1(a)], and E40 [along the pink line in Fig. 1(a)]. The total NRCSs are directly extracted from UAVSAR data. The non-Bragg scattering NRCSs are calculated by using (6) where σ_{VV} and σ_{HH} are the observations and r_B is estimated by (7). As the thickness of the emulsions in Fig. 1(a) is far smaller than the penetration depth of a L band radar, the dielectric constant of clean seawater is used in the calculation of non-Bragg scattering NRCSs. The wind conditions are set to be the same as the wind conditions at the time dataset (a) was collected. The Bragg scattering NRCS is calculated by $(\sigma_{\mathrm{pp}} - \sigma^{\mathrm{nB}})$ in linear units and presented in dB units.

From Fig. 3(a), the NRCSs of total scattering in emulsions-covered areas are smaller than those in the clean sea surface. However, there is no significant difference in the degree of reduction of NRCS by oil spills with different water content. In general, the detection of mineral oils by a SAR is found to be the most efficient for a wind speed of 3–10 m/s. It also may be working at a higher wind speed (10–14 m/s), depending on the type and density of the oil [33]. UAVSAR0626, shown in Fig. 1(a), was acquired at a wind speed of approximately 10–12 m/s, which seems higher than the best detection wind speed. Nevertheless, as shown in Fig. 3(a), the NRCSs of E80, E60, and E40 are significantly smaller than that of the clean sea surface, indicating that the analyses based on UAVSAR0626 are reliable. In Fig. 3(b), the Bragg scattering NRCSs of emulsion-covered sea surfaces are smaller than those of clean sea surfaces, indicating that oil markedly affects Bragg scattering, which is consistent with the results in [26]. As stated in [26], the reductions in the Bragg NRCSs are caused by the suppression of small-scale wind waves. In Fig. 3(c), the reductions in non-Bragg NRCSs related to oil-covered areas are caused by the modification of micro-breaking of cm-dm-scale waves. The microbreaking, which is related to nonlinear features in the profile of decimeter-scale waves, such as bulges, toes, and parasitic capillary ripples [36], [37], can also be effectively suppressed by oil films. Consequently, the NRCSs of both Bragg scattering and non-Bragg scattering of oil-covered sea surfaces are smaller than those of clean sea surfaces. An interesting finding is that the RCNTs of emulsions with different M values (E80, E60, and E40) are similar to that of clean sea surfaces [shown in Fig. 3(d)]. This occurs because the Bragg scattering and non-Bragg scattering attenuated proportions of the sea surface covered by emulsions with different M values are similar. Hence, we can reasonably assume that the RCNT of a thin emulsion-covered sea surface (with arbitrary M), in which case the damping effect dominates in radar backscattering attenuation, is similar to that of a clean sea surface. This

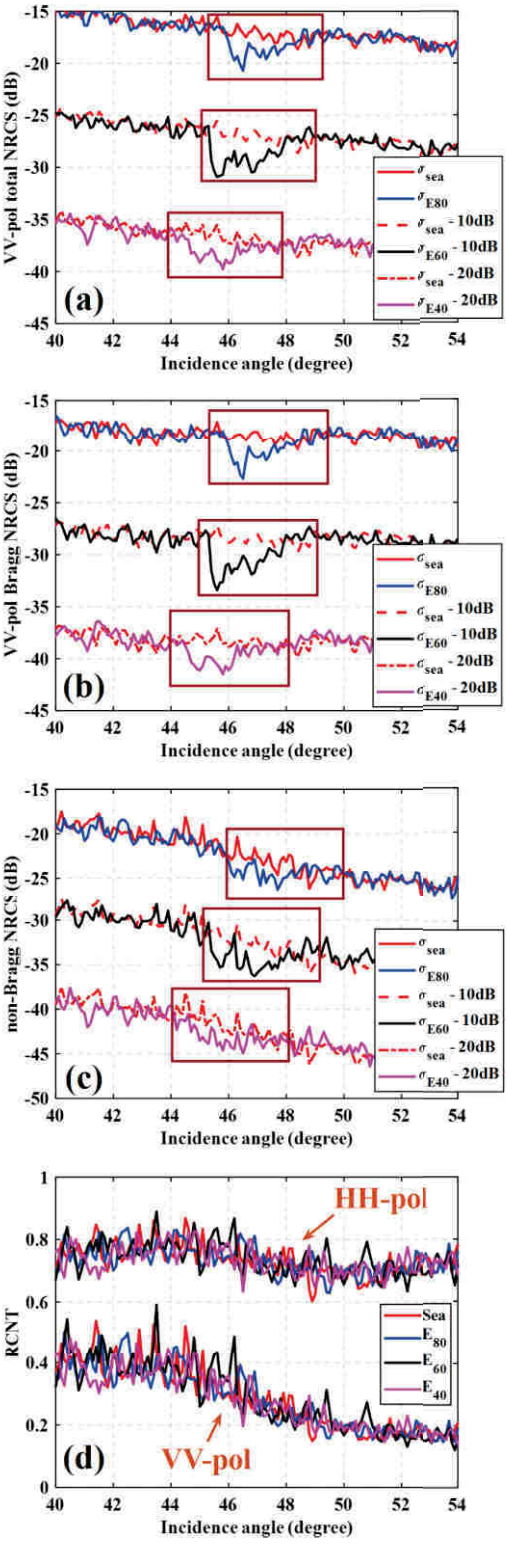

Fig. 3. NRCSs and $c_{\mathrm{pp}}^{\mathrm{nB}}$ of the clean sea, E80, E60, and E40. (a) VV-polarized total NRCSs. (b) VV-polarized Bragg NRCSs. (c) non-Bragg NRCSs. (d) RCNT. In (a) (b), and (c), curves inside the rectangles correspond to the oil spill areas. σ_{sea}, σ_{E80}, σ_{E60} and σ_{E40} correspond to the NRCSs of clean sea, E80, E60, and E40, respectively. An offset of 10 or 20 dB is applied to the results of the E60 and E40 so that it can be more readable. In (d), 'Sea' 'E80' 'E60' and 'E40' correspond to the results of clean sea, E80, E60, and E40, respectively.

assumption is meaningful during the later process of eliminating the influence of non-Bragg scattering.

In the calculation of the curves in Fig. 3, it is assumed that s^2 is the same for a clean sea surface and an oil-covered sea surface. In fact, we still obtain results similar to those in Fig. 3 because s^2 is a filtered MSS which, in L-Band, is mainly sensitive to the waves with wavelengths longer than those which are damped by the oil slick.

C. Impacts of the Effective Dielectric Constant Reduction Induced by Emulsions (or Oil-Water Mixtures) With Different M Values on RCNT

As stated in Section II-B, by replacing the dielectric constant of seawater with the dielectric constant of an oil-water mixture, the Bragg scattering and non-Bragg scattering NRCSs of oil-water mixtures with different M values can be simulated by (2) and (11), respectively. In (11), the parameter q relates to the fraction of the sea surface covered by breaking zones, which is an important parameter for simulating the NRCS of non-Bragg scattering. q is the fraction of the sea surface covered by these areas generated by wave breaking, which is parameterized via the length of the breaking fronts $\Lambda(\mathbf{k}_w)$ of the wind waves [20], [35], [38]

$$q = c_q \int_{k_w < k_{\mathrm{nb}}} k_w^{-1} \Lambda(\mathbf{k}_w) d\mathbf{k}_w \tag{14}$$

where k_w is the wave vector of sea waves, k_{nb} is the upper limit of the range of breaking waves providing non-Bragg scattering. $\Lambda(\mathbf{k}_w)$ is a function of the saturation spectrum parameterized according to (57) in [20]. k_{nb} is the upper limit of the range of breaking waves providing non-Bragg scattering. c_q is a constant of the order on 10. To make the model in agreement with the radar observations, $c_q = 10.5$ was chosen by Kudryavtsev et al. [20]. Therefore, q is an empirical parameter in some sense. More discussions of q can be found in [20], [35], and [38]. According to the research by Kudryavtsev [38], q is 0.03%, 0.21%, and 1.55% at wind speeds of 5, 10, and 20 m/s, respectively, for the L-band. However, if q is set to 0.03% in our simulations (the wind speed of dataset (b) is 2.5–5 m/s), large discrepancies exist between the non-Bragg NRCS estimated by (11) and that derived from dataset (b). Thus, the value of q suggested in [38] is not adopted in this study.

Fig. 4(a) presents the simulated non-Bragg NRCS under various q values and the non-Bragg NRCS of real SAR images. The simulated non-Bragg NRCSs [smooth curves in Fig. 4(a)] are simulated by using (11) and (12). The non-Bragg NRCSs of UAVSAR32010 and UAVSAR14010 (noisy red and black curves) are calculated by (6) and (7) along the white lines in Fig. 1(c) and (d). Fig. 4(a) shows that no single curve matches well with those of UAVSAR32010 and UAVSAR14010. In fact, the value of q in (11) is different from the fraction of the sea surface covered by breaking zones in the general sense. The determination of q is a complex problem, and the influence of oil spills on q is still unclear and requires further study. In our work, to make the model in agreement with the UAVSAR data, $q = 0.014$ is adopted for the following simulations. Fig. 4(b) shows the non-Bragg

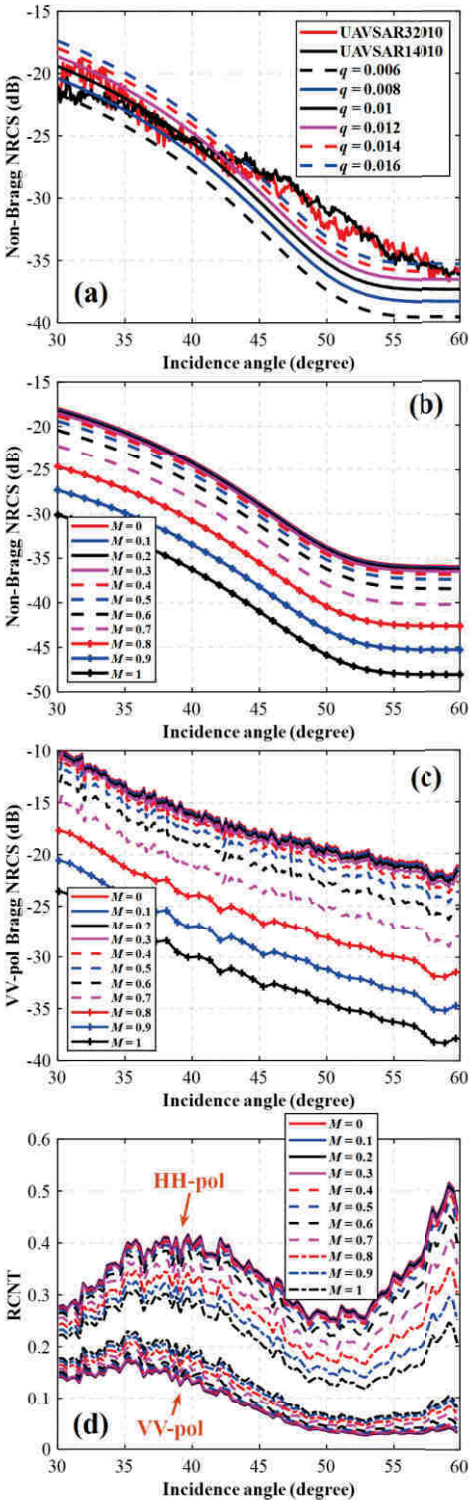

Fig. 4. (a) Comparison of non-Bragg scattering NRCSs simulated by using different q with that derived from UAVSAR32010 and UAVSAR14010. $q = 0.014$ is adopted for the following simulations. (b) Non-Bragg scattering NRCSs simulated with different M values by using (10). (c) VV-polarized Bragg NRCSs simulated with different M values by using (2). In the simulation, the curvature sea spectrum was derived along the white line in Fig. 1(a). (d) RCNTs simulated with different M values by $\sigma^{\mathrm{nB}}/(\sigma^{\mathrm{nB}}+\sigma^{B}_{\mathrm{pp}})$.

scattering NRCSs under various M, which are simulated by using (10)–(12). Fig. 4(c) shows the Bragg scattering NRCSs under various M, which are simulated by using (2)–(5), (9)

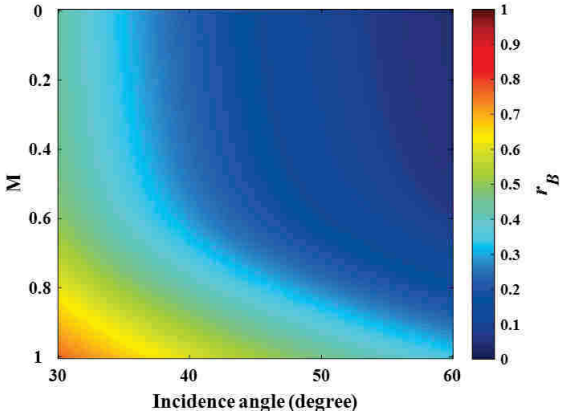

Fig. 5. BPR lookup table corresponds to UAVSAR14010 and UAVSAR32010 under different M values and incidence angles. The BPR increases with M and decreases with incidence angle. Given the incidence angle and PR, M can be determined from this lookup table.

and (10). From Fig. 4(b) and (c), one can see that the impact of M on the non-Bragg and Bragg NRCSs is not obvious when M is smaller than 0.3.

In Fig. 4(d), the RCNT decreases as M increases for HH polarization. Conversely, the RCNT increases as M increases for VV polarization. The VV-polarized RCNT is more sensitive to changes in M than the HH-polarized RCNT. Importantly, both for HH and VV polarizations, the difference in RCNT is not remarkable when M is in the range [0–0.5]. In a real case, crude oils can rapidly form water-in-oil emulsions and the typical values of M are in the range [0.25–0.5] (corresponds to water content in the range of 50% to 75%) [5]. Therefore, we can assume that the RCNT of thick emulsion-covered sea surfaces with different M values, in which case effective dielectric constant reduction dominates for radar backscattering attenuation, is similar to that of a clean sea surface in a real case.

D. Our Approach for Oil-Water Mixture Ratio Retrieval

According to the discussions of Sections IV-B, the RCNT of the emulsion-covered sea surface (with arbitrary M) is similar to that of the clean sea surface in case of the damping effect dominating for radar scattering attenuation [as shown in Fig. 3(d)]. According to the discussions of Sections IV-C, the RCNT of the emulsion-covered sea surface is similar to that of the clean sea surface in the case of the reduction in the effective dielectric constant dominating for radar scattering attenuation and $M < 0.5$ [as shown in Fig. 4(d)]. Considering the typical values of M in real cases are in the range [0.25–0.5], it is reasonable to assume that the RCNT of the oil spill area is equal to that of the clean sea surface in most practical cases. Based on this assumption, the accuracy of a commonly used PR method can be improved by eliminating the influence of non-Bragg scattering. For a given oil spill SAR image, we propose using the following procedures to retrieve M.

1) Establish a lookup table for r_B under different M values and θ_i.
   The r_B under different M values and θ_i are calculated by (7) and (10), and a lookup table for r_B is obtained, denoted as $r_{\mathrm{BM}}(\theta_i, M)$. Notably, in the calculation, the wind speed is set to be the same as the wind speed at the time the dataset was collected [$U_{10} = 5$ m/s for dataset (b)], and the dielectric constant of clean seawater should be replaced by the dielectric constant of the oil-water mixture given in (10).
   The lookup table for r_B corresponding to UAVSAR14010 and UAVSAR32010 is shown in Fig. 5. In the calculation of Fig. 5, the step intervals of discrete θ_i and M are 0.1° and 0.01, respectively.
2) Find the relationship between $c_{\mathrm{pp}}^{\mathrm{nB}}$ and θ_i.
   First, σ_{pp} and θ_i of the pixels of the clean region are directly extracted from the SAR image. In this work, σ_{pp} of clean sea surfaces are extracted along the white lines in Fig. 1(c) and (d). Then, $c_{\mathrm{pp}}^{\mathrm{nB}}$ is estimated by (6) (7), and (8). Finally, to reduce the impact of noise [see the small fluctuations riding on the curves in Fig. 2(e) and (f)] and obtain the relationship between $c_{\mathrm{pp}}^{\mathrm{nB}}$ and θ_i, the least square method is used to fit the curves. The fitting functions ($c_{\mathrm{pp}}^{\mathrm{nB}} = f(\theta_i)$) are plotted in Fig. 2(e) and (f).
   At this step, the relationship function ($c_{\mathrm{pp}}^{\mathrm{nB}} = f(\theta_i)$) between $c_{\mathrm{pp}}^{\mathrm{nB}}$ and θ_i of clean sea surface is obtained. According to the discussion of Section IV-B and C, the $c_{\mathrm{pp}}^{\mathrm{nB}}$ of the oil spill area is equal to that of the clean sea surface in most practical cases. Therefore, the relationship function ($c_{\mathrm{pp}}^{\mathrm{nB}} = f(\theta_i)$) of the clean sea surface is directly applied to the oil spill area in the next step.
3) Find r_B of each pixel in the SAR image.
   Before this process, an empirical threshold is applied on σ_{VV} image to extract the oil spill region from the sea background. σ_{pp} and θ_i of each pixel in the oil region

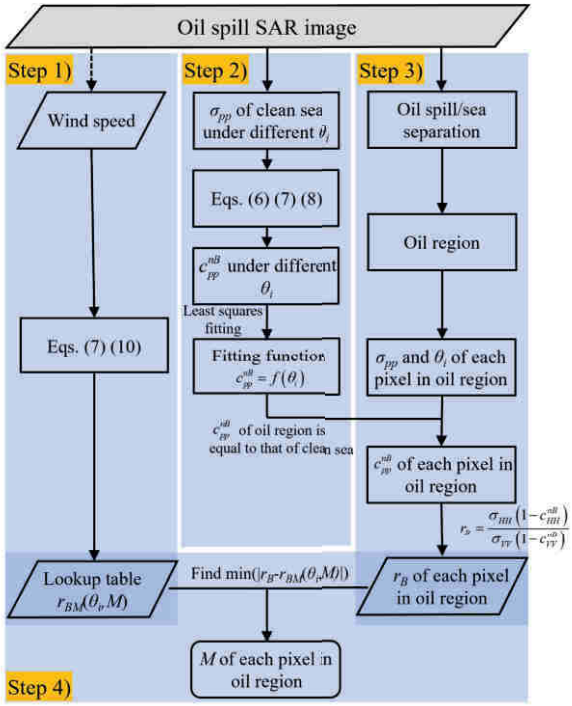

Fig. 6. Flowchart of the proposed method.

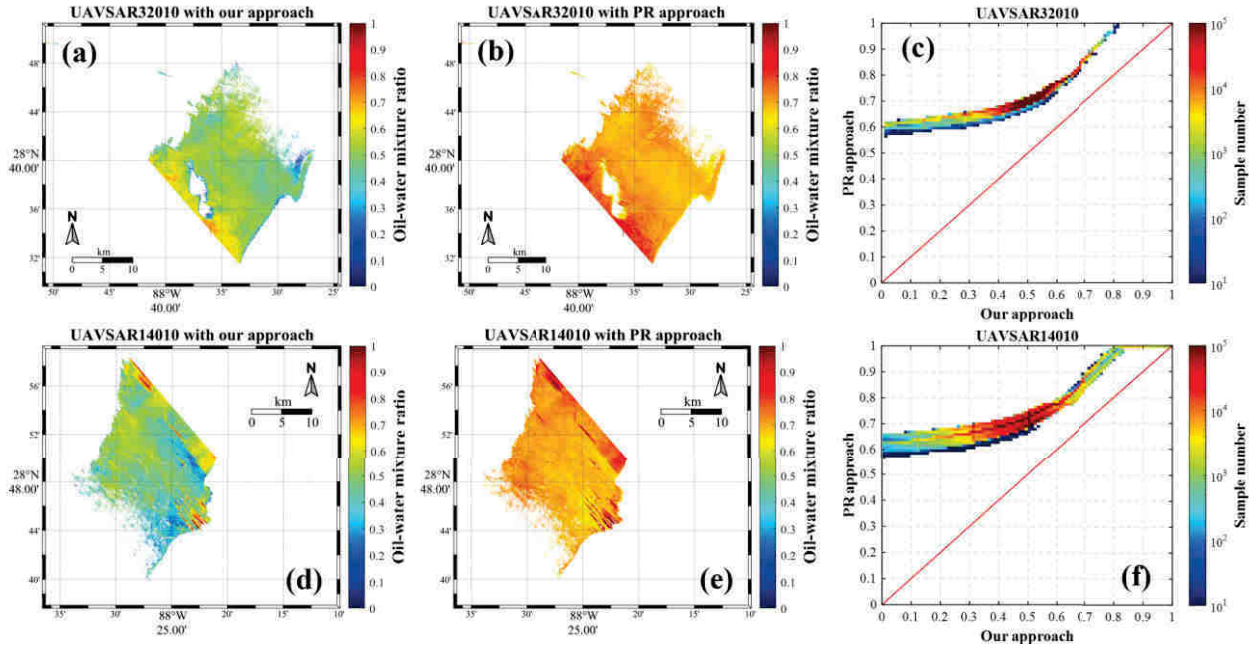

Fig. 7. Inversion results. (a) UAVSAR32010 with our approach. (b) UAVSAR32010 with the traditional PR approach. (d) UAVSAR14010 with our approach. (b) UAVSAR14010 with the traditional PR approach. (c) and (f) Scatter plots of the inversion results for UAVSAR32010 and UAVSAR14010, respectively.

are directly extracted from the SAR image. $c_{\mathrm{pp}}^{\mathrm{nB}}$ of each pixel can be obtained by substituting θ_i of each pixel into ($c_{\mathrm{pp}}^{\mathrm{nB}} = f(\theta_i)$). Thus, r_B of each pixel can be obtained by $r_B = (\sigma_{\mathrm{HH}}(1 - c_{\mathrm{HH}}^{\mathrm{nB}})/\sigma_{VV}(1 - c_{\mathrm{VV}}^{\mathrm{nB}}))$.

4) Determine the M of each pixel.
Comparing the r_B of each pixel (obtained in step 3) with the lookup table ($r_{\mathrm{BM}}(\theta_i, M)$ obtained in step 1), the M of each pixel can be determined by finding the minimum value of $|r_B - r_{\mathrm{BM}}(\theta_i, M)|$.

The proposed method is schematically described in Fig. 6.

Fig. 7 shows the inversion results based on our approach and a traditional PR approach, and the corresponding scatter plots. The traditional PR approach used here contains steps 1), 3) and 4) above. Importantly, in the calculation of the Bragg PR of step 3), the Bragg PR is calculated directly by $\sigma_{\mathrm{HH}}/\sigma_{\mathrm{VV}}$ without eliminating the impact of non-Bragg scattering. As shown in Fig. 7, most of the M calculated by using our approach range from 0.3 to 0.6, while most of the M calculated by the traditional PR approach range from 0.6 to 0.8. In fact, it is difficult to accurately assess the accuracy of our method due to the lack of field-measured M. Therefore, we can only qualitatively evaluate the accuracy of our approach. As mentioned above, the M of oil-in-water emulsions usually ranges from 0.25 to 0.5 under real conditions. Obviously, the inversion results by using our approach match better with those in reality than those of the traditional PR method. Based on the inversion results shown in Fig. 7(a) and (b), on-site disposal workers can take corresponding disposal measures for oil spills with different oil-water mixture ratios.

In response to the DWH accident, 6.977 million liters of dispersant were applied to the sea surface and subsurface near the wellhead [39]. The usage of chemical dispersants may affect the accuracy of inversion results. The impact of a chemical dispersant on the inversion results mainly depends on its dielectric properties. If its dielectric constant is close to that of crude oil, the use of chemical dispersants causes the inversion of M to be larger than the actual value (because the dispersant is treated as crude oil during the inversion process). If the dielectric constant of the dispersant is close to that of seawater, then the use of dispersants has a negligible effect on the inversion results. Unfortunately, as lack of enough information about the dielectric properties and spatial distribution of the dispersant, it is difficult to quantitatively assess the influences of the use of dispersants on the inversion results.

It is worth noting that, the method introduced in this work can be used to determine M based on the fact that the emulsion (or oil-water mixture) is thick enough that it significantly reduces the effective dielectric constant of the sea surface. For a thin oil film whose thickness is significantly smaller than the penetration depth of a radar, the impact of effective dielectric constant reductions on microwave scattering and the Bragg PR is negligible. Therefore, the method proposed in this work cannot be used to retrieve the M of thin oil-water mixtures, for instance, the emulsions in the dataset (a).

Another point to be aware of is that the data used in this work were collected by an airborne SAR whose operating height (approximately 13 800 m) is far less than the height of the ionosphere (approximately 50–1000 km). Therefore, the Faraday rotation mainly induced by the anisotropy in the ionosphere due to charged particles in the presence of a persistent magnetic field [27], [40] makes no impact on radar backscattering and the inversion result. If space-borne low-frequency SAR data [e.g., Phased Array L-band Synthetic Aperture Radar (PALSAR)] are used in the algorithm, the effect of Faraday rotation on SAR data needs to be corrected before the inversion process.

V. Conclusion

Quantitatively estimating the oil-water mixture ratio of marine oil spills by using SAR is of great significance for oil spill traceability and emergency treatment of oil spill pollution. The commonly used PR method for the retrieval of M may not give accurate results due to the significant influence of non-Bragg scattering on microwave scattering. Therefore, a novel BPR method is demonstrated in this work that can improve the accuracy of the retrieved M. The main contributions and conclusions of this article are as follows.

1) By analyzing measured UAVSAR data, it is found that the impact of non-Bragg scattering on the total scattering is remarkable even for the L-band, especially for higher wind speeds. For instance, for $U_{10} = 10$–12 m/s, the HH-polarized RCNT is approximately 0.6–0.8 and the VV-polarized RCNT is approximately 0.1–0.8 varying with the incidence angle. Thus, the impact of non-Bragg scattering is not negligible when retrieving M.
2) By analyzing dataset (a), in which case the damping effect dominates the radar backscattering attenuation, it is found that the RCNTs of the sea surface covered by thin emulsions with different M (0.4, 0.6, and 0.8) are not much different from those of the clean sea surface [see Fig. 3(d)].
3) By simulating the NRCSs of the Bragg scattering, non-Bragg scattering, and RCNTs of sea surfaces covered by thick emulsions (or oil–water mixtures) with different M, in which case the effective dielectric constant reduction dominates for radar backscattering attenuation, it is found that the RCNTs of sea surfaces covered by thick emulsions with different M values are similar to that of clean sea surfaces when $M < 0.5$.
4) By eliminating the impact of non-Bragg scattering, an improved method is proposed for retrieving M. To verify the practicability of the proposed method, it was applied to the UAVSAR images collected during the DWH oil spill accident. The inversion results with our approach show that the M of most oil spill areas ranges from approximately 0.3 to 0.6, which is significantly smaller than that of the traditional PR method (ranging from approximately 0.6 to 0.8). The inversion results obtained by using our approach match better with reality (usually $M = 0.25$–0.5).

Unfortunately, the proposed method has not been verified by field data due to a lack of available field measurements. In fact, this problem also exists in other current similar research work. Therefore, in future work, we hope to have the opportunity to obtain SAR and field synchronization data to verify the algorithm proposed in this article.

Acknowledgment

The authors would like to thank Jet Propulsion Laboratory (JPL), California Institute of Technology for providing the UAVSAR data. H. Zheng would like to thank Dr. Dan Ouyang for her useful advice on improving the quality of this article.

References

[1] F. Mervin and F. Ben, "Water-in-oil emulsions: Formation and prediction," in *Handbook of Oil Spill Science and Technology*, 1st ed., M. Fingas, Ed. Hoboken, NJ, USA: Wiley, 2015, pp. 225–268.

[2] H. Li, W. Perrie, and J. Wu, "Retrieval of oil–water mixture ratio at ocean surface using compact polarimetry synthetic aperture radar," *Remote Sens.*, vol. 11, no. 7, p. 816, Apr. 2019, doi: 10.3390/rs11070816.

[3] S. Skrunes, C. Brekke, C. E. Jones, M. M. Espeseth, and B. Holt, "Effect of wind direction and incidence angle on polarimetric SAR observations of slicked and unslicked sea surfaces," *Remote Sens. Environ.*, vol. 213, pp. 73–91, Aug. 2018, doi: 10.1016/j.rse.2018.05.001.

[4] H. Zheng, J. Zhang, Y. Zhang, A. Khenchaf, and Y. Wang, "Theoretical study on microwave scattering mechanisms of sea surfaces covered with and without oil film for incidence angle smaller than 30°," *IEEE Trans. Geosci. Remote Sens.*, vol. 59, no. 1, pp. 37–46, Jan. 2021, doi: 10.1109/TGRS.2020.2993861.

[5] W. Alpers, B. Holt, and K. Zeng, "Oil spill detection by imaging radars: Challenges and pitfalls," *Remote Sens. Environ.*, vol. 201, pp. 133–147, Nov. 2017, doi: 10.1016/j.rse.2017.09.002.

[6] W. Alpers and H. Hühnerfuss, "The damping of ocean waves by surface films: A new look at an old problem," *J. Geophys. Res.*, vol. 94, no. C5, pp. 6251–6265, May 1989, doi: 10.1029/JC094iC05p06251.

[7] M. Migliaccio, F. Nunziata, and A. Gambardella, "On the co-polarized phase difference for oil spill observation," *Int. J. Remote Sens.*, vol. 30, no. 6, pp. 1587–1602, 2009, doi: 10.1080/01431160802520741.

[8] Z. Honglei, Z. Yanmin, W. Yunhua, Z. Xi, and M. Junmin, "The polarimetric features of oil spills in full polarimetric synthetic aperture radar images," *Acta Oceanol. Sinica*, vol. 36, no. 5, pp. 105–114, 2017, doi: 10.1007/s13131-017-1065-4.

[9] S. Skrunes, C. Brekke, and T. Eltoft, "Characterization of marine surface slicks by radarsat-2 multipolarization features," *IEEE Trans. Geosci. Remote Sens.*, vol. 52, no. 9, pp. 5302–5319, Sep. 2014, doi: 10.1109/TGRS.2013.2287916.

[10] B. Minchew, "Determining the mixing of oil and sea water using polarimetric synthetic aperture radar," *Geophys. Res. Lett.*, vol. 39, no. 16, Aug. 2012, doi: 10.1029/2012GL052304.

[11] M. Collins, M. Denbina, B. Minchew, C. Jones, and B. Holt, "On the use of simulated airborne compact polarimetric SAR for characterizing oil–water mixing of the deepwater horizon oil spill," *IEEE J. Sel. Topics Appl. Earth Observ. Remote Sens.*, vol. 8, no. 3, pp. 1062–1077, Mar. 2015, doi: 10.1109/JSTARS.2015.2401041.

[12] S. Angelliaume, O. Boisot, and C.-A. Guérin, "Dual-polarized L-band SAR imagery for temporal monitoring of marine oil slick concentration," *Remote Sens.*, vol. 10, no. 7, p. 1012, Jun. 2018, doi: 10.3390/rs10071012.

[13] O. Boisot, S. Angelliaume, and C. Guérin, "Marine oil slicks quantification from L-band dual-polarization SAR imagery," *IEEE Trans. Geosci. Remote Sens.*, vol. 57, no. 4, pp. 2187–2197, Apr. 2019, doi: 10.1109/TGRS.2018.2872080.

[14] C. Quigley, C. Brekke, and T. Eltoft, "Retrieval of marine surface slick dielectric properties from Radarsat-2 data via a polarimetric two-scale model," *IEEE Trans. Geosci. Remote Sens.*, vol. 58, no. 7, pp. 5162–5178, Jul. 2020, doi: 10.1109/TGRS.2020.2973724.

[15] C. Quigley, C. Brekke, and T. Eltoft, "Comparison between dielectric inversion results from synthetic aperture radar Co- and quad-polarimetric data via a polarimetric two-scale model," *IEEE Trans. Geosci. Remote Sens.*, vol. 60, pp. 1–18, 2022, doi: 10.1109/TGRS.2020.3038366.

[16] F. Nunziata, A. Gambardella, and M. Migliaccio, "A unitary Mueller-based view of polarimetric SAR oil slick observation," *Int. J. Remote Sens.*, vol. 33, no. 20, pp. 6403–6425, 2012, doi: 10.1080/01431161.2012.687474.

[17] M. Migliaccio and F. Nunziata, "On the exploitation of polarimetric SAR data to map damping properties of the deepwater horizon oil spill," *Int. J. Remote Sens.*, vol. 35, no. 10, pp. 3499–3519, 2014, doi: 10.1080/01431161.2014.905730.

[18] F. Nunziata, C. R. De Macedo, A. Buono, D. Velotto, and M. Migliaccio, "On the analysis of a time series of X–band TerraSAR–X SAR imagery over oil seepages," *Int. J. Remote Sens.*, vol. 40, no. 9 pp. 3623–3646, 2018, doi: 10.1080/01431161.2018.1547933.

[19] S. Angelliaume et al., "SAR imagery for detecting sea surface slicks: Performance assessment of polarization-dependent parameters," *IEEE Trans. Geosci. Remote Sens.*, vol. 56, no. 8, pp. 4237–4257, Aug. 2018, doi: 10.1109/TGRS.2018.2803216.

[20] V. Kudryavtsev, "A semiempirical model of the normalized radar cross-section of the sea surface 1. Background model," *J. Geophys. Res.*, vol. 108, no. C3, pp. FET 2-1–FET 2-24, 2003, doi: 10.1029/2001JC001003.

[21] D. R. Lyzenga, A. L. Maffett, and R. A. Shuchman, "The contribution of wedge scattering to the radar cross section of the ocean surface," *IEEE Trans. Geosci. Remote Sens.*, vol. GE-21, no. 4, pp. 502–505, Oct. 1983, doi: 10.1109/TGRS.1983.350513.

[22] C. Cox and W. Munk, "Slopes of the sea surface deduced from photographs of sun glitter," *Bull. Scripps Inst. Oceanogr.*, vol. 6, no. 9, pp. 401–488, 1956.

[23] V. N. Kudryavtsev, S. Fan, B. Zhang, A. A. Mouche, and B. Chapron, "On quad-polarized SAR measurements of the ocean surface," *IEEE Trans. Geosci. Remote Sens.*, vol. 57, no. 11, pp. 8362–8370, Nov. 2019, doi: 10.1109/TGRS.2019.2920750.

[24] O. M. Phillips, *The Dynamics of the Upper Ocean*. Cambridge, U.K.: Cambridge Univ. Press, 1980.

[25] D. V. Ivonin, S. Skrunes, C. Brekke, and A. Y. Ivanov, "Interpreting sea surface slicks on the basis of the normalized radar cross-section model using RADARSAT-2 copolarization dual-channel SAR images," *Geophys. Res. Lett.*, vol. 43, pp. 2748–2757, Mar. 2016, doi: 10.1002/2016GL068282.

[26] V. N. Kudryavtsev, B. Chapron, A. G. Myasoedov, F. Collard, and J. A. Johannessen, "On dual co-polarized SAR measurements of the ocean surface," *IEEE Geosci. Remote Sens. Lett.*, vol. 10, no. 4, pp. 761–765, Jul. 2013, doi: 10.1109/LGRS.2012.2222341.

[27] C. R. de Macedo, J. C. B. da Silva, A. Buono, and M. Migliaccio, "Multi-polarization radar backscatter signatures of internal waves at L-band," *Int. J. Remote Sens.*, vol. 43, no. 6, pp. 1943–1959, Mar. 2022, doi: 10.1080/01431161.2022.2050435.

[28] T. Meng, X. Yang, K.-S. Chen, F. Nunziata, D. Xie, and A. Buono, "Radar backscattering over sea surface oil emulsions: Simulation and observation," *IEEE Trans. Geosci. Remote Sens.*, vol. 60, pp. 1–14, 2022, doi: 10.1109/TGRS.2021.3073369.

[29] D. Ivonin, C. Brekke, S. Skrunes, A. Ivanov, and N. Kozhelupova, "Mineral oil slicks identification using dual co-polarized Radarsat-2 and TerraSAR-X SAR imagery," *Remote Sens.*, vol. 12, no. 7, p. 1061, Mar. 2020, doi: 10.3390/rs12071061.

[30] M. M. Espeseth, S. Skrunes, C. E. Jones, C. Brekke, B. Holt, and A. P. Doulgeris, "Analysis of evolving oil spills in full-polarimetric and hybrid-polarity SAR," *IEEE Trans. Geosci. Remote Sens.*, vol. 55, no. 7, pp. 4190–4210, Jul. 2017, doi: 10.1109/TGRS.2017.2690001.

[31] A. G. Voronovich and V. U. Zavorotny, "Theoretical model for scattering of radar signals in Ku- and C-bands from a rough sea surface with breaking waves," *Waves Random Media*, vol. 11, no. 3, pp. 247–269, Jul. 2001, doi: 10.1080/13616670109409784.

[32] S. Skrunes, C. Brekke, C. E. Jones, and B. Holt, "A multisensor comparison of experimental oil spills in polarimetric SAR for high wind conditions," *IEEE J. Sel. Topics Appl. Earth Observ. Remote Sens.*, vol. 9, no. 11, pp. 4948–4961, Nov. 2016, doi: 10.1109/JSTARS.2016.2565063.

[33] B. Minchew, C. E. Jones, and B. Holt, "Polarimetric analysis of backscatter from the Deepwater Horizon oil spill using L-band synthetic aperture radar," *IEEE Trans. Geosci. Remote Sens.*, vol. 50, no. 10, pp. 3812–3830, Oct. 2012, doi: 10.1109/TGRS.2012.2185804.

[34] H. Zheng, J. Zhang, A. Khenchaf, and X.-M. Li, "Study on non-Bragg microwave backscattering from sea surface covered with and without oil film at moderate incidence angles," *Remote Sens.*, vol. 13, no. 13, p. 2443, Jun. 2021, doi: 10.3390/rs13132443.

[35] V. Kudryavtsev, "A semiempirical model of the normalized radar cross section of the sea surface, 2. Radar modulation transfer function," *J. Geophys. Res.*, vol. 108, no. C3, pp. FET 3-1–FET 3-16, 2003, doi: 10.1029/2001JC001004.

[36] S. A. Ermakov et al., "Remote sensing of organic films on the water surface using dual co-polarized ship-based X-/C-/S-band radar and TerraSAR-X," *Remote Sens.*, vol. 10, no. 7, p. 1097, Jul. 2018, doi: doi:10.3390/rs10071097.

[37] I. A. Sergievskaya, S. A. Ermakov, A. V. Ermoshkin, I. A. Kapustin, O. V. Shomina, and A. V. Kupaev, "The role of micro breaking of small-scale wind waves in radar backscattering from sea surface," *Remote Sens.*, vol. 12, no. 24, p. 4159, Dec. 2020, doi: 10.3390/rs12244159.

[38] V. Kudryavtsev, "On radar imaging of current features: 1. Model and comparison with observations," *J. Geophys. Res.*, vol. 110, no. C7, p. 07016, 2005, doi: 10.1029/2004jc002505.

[39] J. Mathew et al., "Dioctyl sulfosuccinate analysis in near-shore Gulf of Mexico water by direct-injection liquid chromatography–tandem mass spectrometry," *J. Chromatography A*, vol. 1231, pp. 46–51, Mar. 2012, doi: 10.1016/j.chroma.2012.01.088.

[40] F. J. Meyer and J. B. Nicoll, "Prediction, detection, and correction of Faraday rotation in full-polarimetric L-band SAR data," *IEEE Trans. Geosci. Remote Sens.*, vol. 46, no. 10, pp. 3076–3086, Oct. 2008, doi: 10.1109/TGRS.2008.2003002.